Process Biochemistry 64 (2018) 63–73

Contents lists available at ScienceDirect

Process Biochemistry

journal homepage: www.elsevier.com/locate/procbio

Expression, purification, and preliminary characterization of human presenilin-2

Ge Yang[a,b,1], Kun Yu[a,b,1], Jan Kubicek[c], Jörg Labahn[a,b,*]

[a] Centre for Structural Systems Biology (CSSB), CSSB-FZJ, Notkestr. 85, 22607 Hamburg, Germany
[b] Institute of Complex Systems-Structural Biochemistry (ICS-6), Forschungszentrum Jülich, Wilhelm-Johnen-Str., 52425 Jülich, Germany
[c] Cube Biotech GmbH, Alfred-Nobel-Str. 10, 40789 Monheim, Germany

ARTICLE INFO

Keywords:
Presenilin-2
Expression
Purification
Secondary structure
Tertiary structure
Thermal stability

ABSTRACT

Presenilins (PS1 and PS2) exhibit similar γ-secretase-dependent and −independent functions with subtle variations. In this study, we established a cost-effective process to overexpress and purify full-length human PS2 in sufficient quantities and quality for structural studies. Upon optimization, milligram quantities of homogeneous trimeric hisPS2 were purified, which enabled the preliminary characterization of human hisPS2 zymogen. Far-UV and near-UV CD as well as fluorescence spectroscopy revealed that purified hisPS2 contained the expected secondary structure and was folded into a defined tertiary structure. Thermal stability analysis revealed a T_m value of ~55 °C for secondary structure while cholesterol significantly increased the stability. The low melting temperature of ~34 °C for the tertiary structure was able to explain the purity and aggregation problems observed during purification. Additionally, the occurrence of calcium ions induced structural changes to different extents for PS2WT and PS2-D263A/D366A was observed, which is consistent with previous studies.

1. Introduction

Full-length presenilin zymogens (PS1 and PS2) are short-lived multi-transmembrane proteins found in the endoplasmic reticulum (ER) [1]. During ER-to-Golgi recycling [2], PS zymogens are activated by autocleavage into stable N- and C-terminal fragments that associate with three other components – nicastrin, Aph1, and Pen-2–to form the γ-secretase complex [3,4]. In contrast to endogenous PS1, PS2 was mainly found as the full-length protein in human and mouse brains [5,6]. During embryonic development [7], neuron maturation [6], and aging [8], PS1 expression was either constant or decreased while PS2 expression increased, thus indicating their distinct regulatory functions.

Due to the existence of two PSs and – in humans – two APH1 isoforms, at least four complexes co-exist in the cell [9,10], which process distinct substrates depending on their subcellular localization [9]. The PS1-containing complexes reside predominantly at the recycling endosomes and the plasma membrane [11,12], while PS2-containing complexes are restricted to late endosomes and lysosomes [13]. PSs exhibit similar but subtly distinctive biological functions in γ-secretase-dependent and –independent pathways [14].

The most widely studied γ-secretase substrates are Notch and C-terminal fragments of β-amyloid precursor protein (APP-CTFs). The cleavage of Notch by γ-secretase releases the intracellular domain to the nucleus, which in turn affects the development of cells and cancer [15]. The cleavage of APP-C99 by γ-secretase generates amyloid-beta peptides (Aβ) of varying lengths, among which the longer peptides – particularly Aβ42 and Aβ43–are aggregation-prone and are the initial and key components of Aβ plaques [16], a hallmark of Alzheimer's disease (AD). According to the amyloid hypothesis of AD, mutations in APP or PSs induce the relatively elevated production of Aβ42 peptides. The abnormal deposition of Aβ42 was proposed to trigger the AD pathogenesis [17,18]. Of all the PS-related AD pathogenic mutations, about 150 are found in PS1 and about 13 in PS2 [19]. PS1-containing γ-secretase was reported to produce more Aβ than PS2-containing γ-secretase [20] and is responsible for the production of the majority of CNS Aβ [21]. However, familial AD (FAD) mutations in PS2 increase the production of intracellular toxic Aβ42 in late endosomes and lysosomes. Some FAD-PS1 mutations lead to a change in the subcellular location of γ-secretase and phenocopy the FAD-PS2 mutations [13]. The amyloid hypothesis is challenged by the heterogeneous clinical phenotypes of PS mutations and is yet to be experimentally proven [22–24]. The presenilin hypothesis of AD proposes that the loss of

Abbreviations: PS1 or PS2, presenilin-1 or presenilin-2; AD, Alzheimer's disease; APP, β-amyloid precursor protein; Aβ, amyloid beta peptide; IPTG, Isopropyl β-D-1-thiogalactopyranoside; PMSF, phenylmethylsulfonyl fluoride; FC14, Fos-choline-14; CHS, cholesteryl hemisuccinate tris salt; CD, circular dichroism; T_m, melting temperature

* Corresponding author at: Centre for Structural Systems Biology (CSSB), CSSB-FZJ, Notkestr. 85, 22607 Hamburg, Germany.
E-mail address: j.labahn@fz-juelich.de (J. Labahn).
[1] Authors contributed equally.

http://dx.doi.org/10.1016/j.procbio.2017.09.012
Received 6 January 2017; Received in revised form 18 August 2017; Accepted 11 September 2017
Available online 12 September 2017

essential functions of PSs alone might be a more potent cause of AD-related phenotypes than the accumulation of toxic Aβ peptides [25,26]. It is still debated as to whether PS mutations induce AD through gaining a toxic function of γ-secretase or through the loss of an essential function of PSs.

PSs are also proposed to be involved in many other biological processes independent of γ-secretase, including the modulation of intracellular calcium homeostasis although the exact site(s) and mechanism of this function requires further investigation. It was suggested that PS holoproteins form ER channels [27,28], but contradicting results have been reported [29–31]. This calcium leakage function is independent of γ-secretase activity: PS1-D257A, which lacks proteolytic activity and therefore remained uncleaved, still exhibited the channel function [28]. PSs physically interact with ER calcium channels (e.g. InsP3R [29,32] and RyR [33,34]) and up-regulate calcium release. Furthermore, PSs affect the calcium influx by interacting with the ER SERCA pump [35,36]. For PS2, it is only the full length protein and not the cleaved fragments that exhibits depleting effects on the intracellular calcium stores [36]. The preferential interaction of PS2 with calcium binding proteins (e.g. calmyrin [37], μ-calpain [38], and sorcin [39]) were also observed. PS2–but not PS1–was also reported to modulate ER-mitochondria tethering and calcium cross-talk between these two organelles [40,41]. PSs are also essential in regulating mitochondrial calcium homeostasis [42]. Moreover, PSs also alter lysosomal calcium release/storage [43,44]. Many familial AD mutations in PSs cause disturbed calcium signaling, which may indicate an important role for abnormal calcium signaling in AD pathogenesis [45–47].

Among the PS-related structural information reported were the crystal structure of the presenilin archaeal bacterial homolog (PSH) [48] and the nuclear magnetic resonance (NMR) structures of the C-terminal domains of PS1 (PS1-CTD) [49] and the cryo-electron microscopy (cryo-EM) structures of PS1-containing γ-secretase [50–52]. These analyses are all based on activated PS1. The low expression level and poor solution behavior of full-length eukaryotic PSs [48] directed research towards bacterial homologues. Structural information on the PS2 zymogen alone may help to elucidate the different physiological and pathological functions of PS1 and PS2, and might also shed light on the auto-inhibition and activation mechanisms for both the proteolytic activity of γ-secretase and the suggested passive calcium leakage channel.

The present study reports on the detailed process for large-scale expression, purification, and preliminary structural characterization of human PS2 by CD spectroscopy. This expression and purification approach allows milligram quantities of well-folded, homogeneous full-length PS2 zymogens to be obtained for further structural analysis.

2. Materials and methods

2.1. Materials

The *E. coli* strain BL21-CodonPlus (DE3)-RP was obtained from Agilent Technologies (Hamburg, Germany), BL21 Star™ (DE3) from Invitrogen (Darmstadt, Germany), C41(DE3) and C43(DE3) from Lucigen (Heidelberg, Germany), detergents and cholesterol from Anatrace (Maumee, USA) and Glycon (Luckenwalde, Germany), Ni-NTA resin from Qiagen (Hilden, Germany), and the EDTA-free protease inhibitor cocktail from Roche (Basel, Switzerland). Furthermore, the HiLoad 16/60 Superdex 200 pg column was obtained from GE Healthcare (Freiburg, Germany). All other reagents were purchased from either Sigma-Aldrich or Merck.

2.2. Plasmids construction

A codon usage-optimized human PS2 gene was synthesized by GENART (Regensburg, Germany) and cloned into the pQE2 vector (Qiagen, Hilden, Germany) with an N-terminal hexa-histidine (hisPS2). PS2 active site mutations (hisPS2-D263A/D366A) were performed using the QuikChange Site-Directed Mutagenesis Kit (Agilent Technologies, Hamburg, Germany). The correctness of resulting plasmids was confirmed by sequencing.

Initially, the possibility of expressing and purifying the entire PS2 in *E.coli* was evaluated using a PS2 construct with N-terminal hexa-histidine and a C-terminal strep tag (hisPS2strep), which allowed protein integrity to be monitored by western blot.

2.3. Expression and membrane preparation

An overnight pre-culture (supplemented with 50 μg/ml kanamycin and 2% (w/v) glucose) was diluted into 300 ml Terrific Broth (TB) or Double Yeast Tryptone (DYT) media in a 2 l flask to an OD_{600} of ~ 0.2 and grown at 30 °C to an OD_{600} of ~ 0.8 for induction with 0.2 mM IPTG. Cells were then grown at 18 °C for 16 h before being pelleted. The removal of the periplasmic fraction was performed after harvesting [53].

The obtained pellet was resuspended with 10 ml ice-cold lysis buffer (20 mM Tris·HCl; pH 8.0; 10% (v/v) Glycerol; Protease inhibitor 1 tablet/50 ml buffer; 1 mM PMSF; 1 mg/ml Lysozyme; DNAse 5 mg/50 g cell pellet; 1 mM TCEP) per gram pellet and incubated at 4 °C for 1 h under gentle stirring. The cell suspension was passed through a cell disruptor (EmulsiFlexC3, Avestin, Mannheim, Germany) five times at a pressure of ~ 20, 000 psi. After lysis, EDTA (10 mM) and NaCl (300 mM) were added to the lysate. This suspension was subjected to three steps of sequential centrifugations at 4 °C: 900*g* (15 min), 10, 000 × g (30 min), and 100, 000 × g (1 h). The pellet fraction from the second (inclusion body fraction) and third centrifugation step (membrane fraction) were analyzed by western blot.

2.4. Solubilization screening

Membrane from 0.1 g cell pellet was suspended in 0.5 ml solubilization buffer (20 mM Tris·HCl, pH 8.0; 10% (v/v) Glycerol; 300 mM NaCl; 1 mM PMSF; Protease inhibitor 1 tablet/50 ml buffer; 1 mM TCEP; 1–2% (w/v) detergent). The detergents used in the study are indicated in Table 1 in Ref. [54]. After solubilization, the supernatant and pellet were separated by centrifugation at 100,000*g* for 1 h and analyzed by western blot.

2.5. Ni-NTA purification

Membrane from 20 g cell was solubilized in 100 ml solubilization buffer (1% (w/v) Fos-choline-14 (FC14)). After centrifugation, imidazole was added to the supernatant to 15 mM. This solution was loaded onto a 5 ml pre-equilibrated Ni-NTA column. The flow-through was collected and reapplied to the column twice. Five column volumes (CV) of the solubilization buffer supplemented with 15 mM imidazole (wash 1) were then passed through the column. After this step, the detergent concentration was decreased to 0.014% (w/v) FC14. Other components of the buffer were kept constant except for changes in salt and imidazole concentrations: wash 2 (500 mM NaCl, 5 CV), wash 3 (1 M NaCl, 5 CV), wash 4 (20 mM imidazole), and wash 5 (25 mM imidazole) were carried out sequentially. Elution of the bound protein was achieved by the buffer being supplemented with 300 mM imidazole. For solubilization and purification of hisPS2 in mixed micelles of FC14 and cholesterol, cholesteryl hemisuccinate tris salt (CHS) was added to the corresponding buffers (CHS: FC14 = 1:10 (w/w)).

2.6. Mass spectroscopy (MS)

Bands of interest were cut from SDS-PAGE, destained, dehydrated, and digested as described in the Trypsin Profile IGD Kit (Sigma-Aldrich, Hamburg, Germany). 0.1% TFA was added to the extraction for acidification prior to matrix addition. The digested peptides were then

analyzed by matrix-assisted laser desorption/ionization time-of-flight (MALDITOF) and MS/MS using a Bruker Daltonics Ultraflex III TOF/TOF mass spectrometer (Bruker Daltonics, Billerica, USA). Baseline correction and mass peak detection were performed using the software flex Analysis Version 3.0 (Build 92, Bruker Daltonics, Billerica, USA). Finally, both the MS and tandem MS data were searched against Swiss-Prot protein databases for protein identification.

2.7. Size exclusion chromatography (SEC)

2 ml of concentrated protein sample (30 KDa Millipore concentrator, Millipore, Darmstadt, Germany) was filtrated (0.2 μM centrifugation filter, Nanosep®, Dreieich, Germany) and subjected to SEC on a superdex 200 pg column calibrated by a SEC calibration kit (Sigma-Aldrich, Hamburg, Germany). The flow rate used was 0.3 ml/min. Detergent micelles were visualized by staining FC14 micelles by rhodamine B (Avanti Polar Lipids, Hamburg, Germany) at a monomer mole ratio of ~20:1. The apparent molecular weight and radius of the eluted protein-detergent complex were obtained from the calibration curve.

2.8. Circular dichroism (CD) and fluorescence spectroscopy

The CD and fluorescence spectra were recorded using an Aviv 425 circular dichroism spectrometer (Aviv Biomedical, Lakewood, USA) equipped with fluorescence emission scanning monochromator which enables the simultaneous collection of CD and fluorescence data. Purified hisPS2 was buffer exchanged by a PD-10 desalting column (GE Healthcare, Freiburg, Germany) into CD buffer (10 mM sodium phosphate, pH 7.4, 0.014% (w/v) FC14) for data collection. For far-UV CD, spectra between 260 nm and 185 nm were collected with 1 nm step size, 1 nm bandwidth, and 9 s averaging time in 0.1 cm path length Suprasil cuvettes. For near-UV CD, data from 350 nm to 250 nm were obtained with 0.25 nm step size, 1 nm bandwidth, and 30 s averaging time in 1 cm path length cuvettes. Baselines were measured from buffer solutions under the same experimental conditions. Baseline subtraction and spectra smoothing were carried out using the Aviv CDS software. All spectra were recorded in triplicate and collected at 4 °C except the thermal unfolding experiments. The protein concentrations used for far- and near-UV CD were ~ 3.3 μM and ~ 20.8 μM, respectively. Protein concentrations were determined from the absorbance at 280 nm using the calculated extinction coefficient 76780 $M^{-1} cm^{-1}$ obtained by ExPASy ProtParam [55]. The baseline-subtracted spectra were scaled to obtain the mean residue ellipticy (MRE) using a mean residue weight of 112.54 Da. The CDSSTR algorithm and the reference data sets 4, 7, and SMP 180 were used for the deconvolution of spectra [56,57].

During thermal unfolding, the temperature was raised in 2 °C steps with at a heating rate of 0.5 °C/min and 1 min equilibration time before data collection. For far-UV CD, the signal at 221 nm was collected with an averaging time of 9 s between 4 °C and 98 °C. A temperature reverse scan was carried out in order to investigate the reversibility. For near-UV CD, the 292 nm signals were recorded with an averaging time of 30 s from 4 °C to 80 °C. The measured signals were corrected for buffer contribution and fitted with a Boltzmann sigmoidal equation (Origin 9.0) to obtain the melting temperature (T_m).

The fluorescence emission spectra (450 nm to 270 nm) were recorded at different excitation wavelengths with a bandwidth of 2 nm, a photomultiplier tube (PMT) voltage of 900, an averaging time of 1 s, and an emission slit setting of 2 mm.

3. Results

3.1. Overexpression of hisPS2

Heterologous overexpression of human membrane proteins often result in cell death, protein misfolding, and aggregation due to the saturation of the host sorting and translocation system and cell membranes [58,59]. We therefore applied codon usage-optimized DNA and screened four different strains in DYT and TB media for their ability to overexpress human PS2.

(a)

Groups	Induction OD 600	OD 600 after 16 h	Pellet (gram)
DYT+ C43	0.81	4.45	1.01
DYT+ C41	0.83	4.63	1.09
DYT+STAR	0.83	0.22	n.d
DYT+ RP	0.63	0.21	n.d
TB+ C43	0.76	6.02	1.49
TB+ C41	0.78	4.88	1.25
TB+ STAR	0.63	0.99	n.d
TB+ RP	0.62	4.23	0.93

(b)

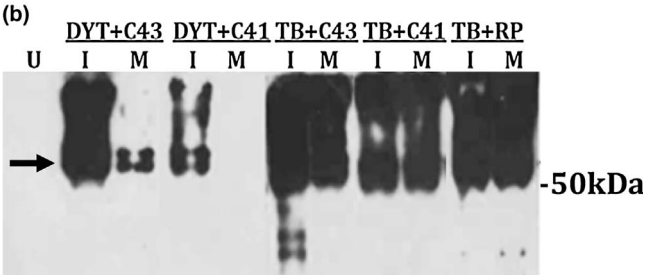

Fig. 1. Expression screening of hisPS2 in different cells and media.
(a) Expression screening was performed in 100 ml DYT or TB media with four different strains (see Section 2.1). The OD600 at induction and after 16 h expression as well as the wet cell pellet weight are listed. Experiments with OD600 lower than 1 were not analyzed (n.d. = not determined). (b) Western blot analysis of expression. U: uninduced control; I: inclusion body fraction; M: membrane fraction. 10 μg total protein was loaded in each lane for comparison. N-terminal his-tag was investigated by monoclonal anti-poly-histidine-HRP antibody (Sigma-Aldrich, Hamburg, Germany). The black arrow points to the monomeric form of hisPS2.

As listed in Fig. 1a, hisPS2 exhibited toxicity to STAR and RP strains, resulting in cell death (OD600 lower than induction) after 16 h expression when the DYT medium was used − but not for the TB medium. This is probably due to the acidic stress upon overexpression [59]. For the DYT medium, an acidic pH was observed upon cell harvesting. Regardless of the medium used, C41 and C43 strains yielded relatively higher cell densities than the other two strains. These strains contain mutations in the lacUV5 promoter which slows down the speed of protein translation [60]. Meanwhile, a lower temperature (18 °C) after induction was used to further slow down the protein expression rate, which allows the translation system to optimally adapt to induction stress [61]. It was revealed by means of Western blot (Fig. 1b) on the N-terminal his-tag that most protein was present in the inclusion body fraction when the DYT medium was used. For the TB medium, an equal distribution of the protein between the inclusion bodies and the membrane fraction was found. In order to obtain the correctly folded protein, only the isolated membrane fraction was used for extraction of hisPS2. Large-scale overexpression of hisPS2 was achieved in the C43 (DE3) strain with the TB medium. This combination yielded the highest cell density and cell pellet weight. Typically, after 16 h of expression, an OD 600 of 8.3 ± 0.3 and a cell pellet wet weight of 12.9 ± 0.3 g/L was obtained.

3.2. Fos-choline detergents are most efficient in solubilizing hisPS2

After overexpression, we investigated the ability of 13 detergents with different soluble groups, charge, and chain length to solubilize hisPS2 (Table 1 in Ref [54]). After detergent extraction (Fig. 2a), clear, transparent residual pellets were observed for FC12, FC14, FC16, and NLS. The other detergents exhibited pellets that were brown in color. Western blots (Fig. 2b) revealed that the signal in the supernatant (SN)

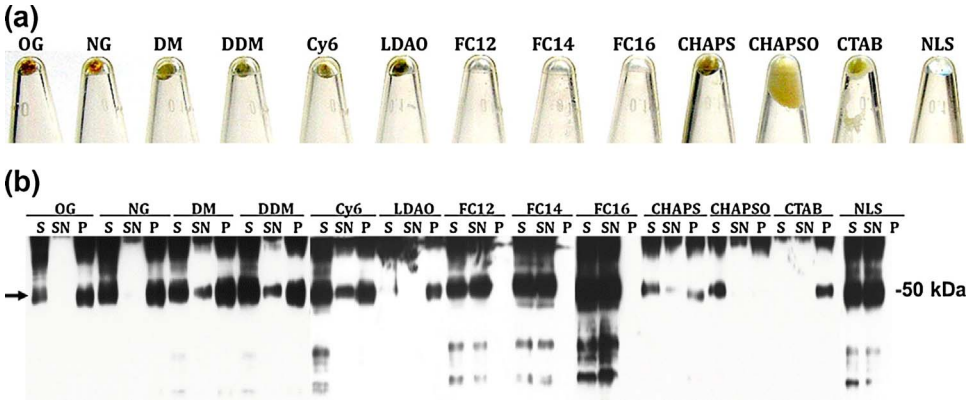

Fig. 2. Effect of detergents on solubilization of hisPS2.
Membrane suspensions corresponding to identical amounts of cell pellets were solubilized with different detergents (see Section 2.4). Residual membrane pellets after detergent extraction (a) and western blot analysis of detergent screening (b) are shown. Each lane was loaded with an amount corresponding to 3.4 mg of cell pellet. S: suspension before 100,000 × g; SN: supernatant after 100,000 × g; P: pellet after 100,000 × g. The full name of detergents are listed in Table 1 in Ref [54]. N-terminal his-tag was investigated by monoclonal anti-polyhistidine-HRP antibody (Sigma-Aldrich, Hamburg, Germany). The black arrow points to the monomeric form of hisPS2.

after centrifugation was comparable to the total signal found for the suspension (S) before centrifugation for FC12, FC14, FC16, and NLS. No protein signal was detected in the pellets for these four solubilizers. Other detergents investigated solubilized hisPS2 either poorly or not at all. It was generally observed that the less brown the color of the pellet after detergent extraction, the more efficient the solubilization was. The common denominator for complete solubilization was detergents with an aliphatic chain length of at least 12 carbons and the presence of negative charge at the head group.

3.3. Purification of hisPS2 from membrane fraction by Ni-NTA and SEC

The small-scale purification of hisPS2 by Ni-NTA or a combination of Ni-NTA and Strep-Tactin purification for hisPS2strep was performed in the presence of different detergents (data not shown). It was observed that Ni-NTA binds hisPS2 more tightly than Strep-Tactin. Ni-NTA resin was therefore used for the capturing step of purification. FC14 was chosen as the purification detergent. Different amounts of FC14 micelles and Ni-NTA matrix were used with a constant amount of cell pellets to investigate the best yield and purity (data not shown). 5 ml 1% (w/v) FC14 and 0.25 ml Ni-NTA matrix per gram of cell pellet gave the best result. SDS-PAGE exhibited two dominant bands of PS2 and impurities in the elution fractions (Fig. 3a). The two dominant bands were found to contain PS2 by MS based on five identified peptides (Fig. 1 in Ref [54]) with 14% sequence coverage (Fig. 3b). All the peptides detected belong to extra-membrane segments (Fig. 2 in Ref [54]), which is similar to the MS result reported for PS1 [62]. The low sequence coverage in MS is probably a result of the inaccessibility of the cleavage sites due to bound detergent. Despite repeated attempts to improve the sequence coverage, only a segment of TM7 was detected (data not shown). ImageJ was used to quantify the intensities of the Coomassie-stained bands. The purity after Ni-NTA was calculated at ~ 81% (Fig. 3a).

After Ni-NTA chromatography, minor impurities and aggregated hisPS2 were removed by SEC. HisPS2 was distributed into two major peaks with a shoulder on the left side of the first peak (Fig. 4a). The pooled fraction of the first peak not only contained hisPS2 but also an *E.coli* protein of ~75 kDa, as detected by SDS-PAGE (Fig. 4a, inset, lane1). The purity of the pooled fractions from the second peak was estimated at ~ 95% via ImageJ by quantifying the intensity of blue-silver-stained bands (Fig. 4a, inset, lane2). Fractions from the second peak were collected and again subjected to SEC. The Gaussian-shaped peak indicated a monodispersed protein detergent complex (Fig. 4b) at an elution volume of 67.9 ml, which corresponded to a radius of 5.3 nm (Fig. 4c). This radius indicated the insertion of protein into the detergent micelles. The elution volume of rhodamine B-stained empty FC14 micelles at 79.9 ml corresponded to a radius of 3.7 nm (Fig. 4c), whereas FC14 micelles were reported as having a hydrodynamic radius of 3.2 nm [63]. The value found here is in agreement with the reported value considering the differences in methods, conditions, and the

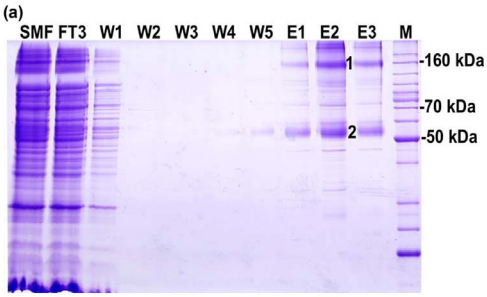

(b)

Bands	Protein	% of the sequence coverage	Mascot score	RMS error
1	PS2	14 %	71	5
2	PS2	14 %	79	3

Fig. 3. Ni-NTA purification and identification by mass spectrometry.
(a) SDS-PAGE (12%, Coomassie staining) analysis of Ni-NTA purification fractions. SMF: solubilized membrane fraction; FT: flow through; W: wash; E: elution; M: BenchMark Protein Ladder (Invitrogen, Darmstadt, Germany). The numbers on the right side of the bands indicate the protein bands which were excised and subjected to mass spectrometry (see Section 2.6). (b) Mass spectrometry of purified hisPS2. The MS data were searched against the Swiss-Prot database for identification. The excised bands were identified as human PS2 with 14% sequence coverage.

staining of micelles. By correcting the apparent molecular weight of the hisPS2-FC14 complex (185.3 kDa, Fig. 4d) for the empty FC14 micelles (47 kDa, Anatrace), hisPS2 was calculated to form trimers in FC14 micelles. Therefore, from 1 l culture, 1.05 ± 0.12 mg homogeneous trimeric hisPS2 was obtained by a combination of Ni-NTA and SEC (Fig. 4e).

Before delipidation of the solubilized membrane proteins by the washing steps during Ni-NTA chromatography, the detection of hisPS2 was poor in western blots. It was thus not possible to establish reliable estimates of the expression level. We therefore used a relative recovery that linked yields of hisPS2 under native purification conditions to yields from the same procedure, but using denaturing conditions throughout (6 M urea, 1% NLS). A relative recovery of 90% was calculated for the ratio between the yields from native and denaturing purification under the final protocol.

On 12% SDS-PAGE (Fig. 3a), hisPS2 exhibited an apparent Mw of ~50 kDa and ~145 kDa for the oligomer band, whereas on 10%, SDS-PAGE (Fig. 4a, inset), the higher Mw band appeared reproducibly at ~100 kDa. This type of Mw shift for helical membrane proteins dependent on the acrylamide concentration has been previously studied and reported [64]. At ~50 kDa, two diffuse bands were observed on 10% SDS-PAGE (Fig. 4a), but not on 12%. The three bands in Fig. 4b

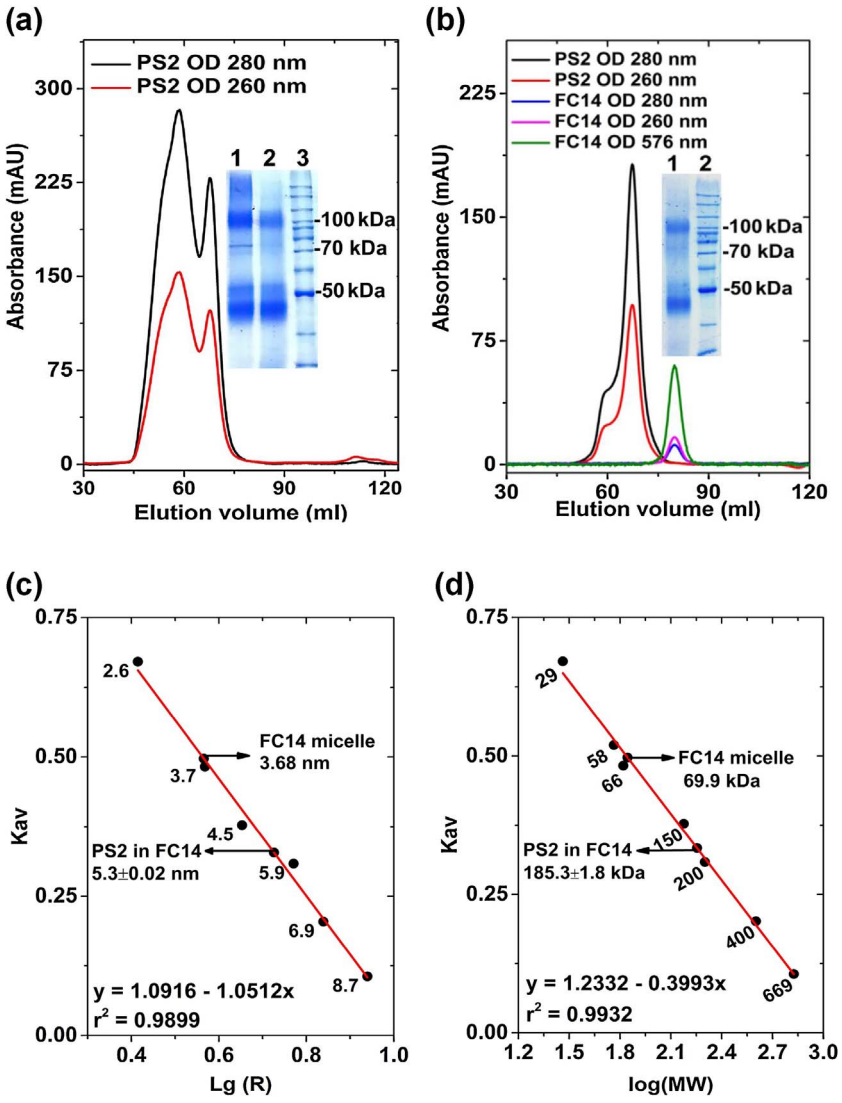

Fig. 4. SEC purifications of hisPS2 after Ni-NTA.
(a) Ni-NTA elution was concentrated and subjected to SEC. Inset: 10% SDS-PAGE analysis of SEC fractions (blue-silver staining). Lane 1: hisPS2 from first peak; lane 2: hisPS2 from second peak; lane 3: BenchMark Protein Ladder. (b) The right half of the second main peak from (a) was pooled and again subjected to SEC. The SEC profile of rhodamine B-stained empty FC14 micelles (green, magenta, and blue curves) was overlaid. Inset: 10% SDS-PAGE analysis of purified hisPS2; lane 1: purified hisPS2 from main peak; lane 2: BenchMark Protein Ladder. (c) Radius determination by calibration curve for dependence of partition coefficient (K_{av}) from log of radii of protein standards. (d) Molecular weight determination by calibration curve of K_{av} against log of molecular weight from protein standards. (e) Purification table for optimized purification protocol of hisPS2 from 20 g cell (~1.5 l culture). [a] Protein purity was determined by densitometric analysis of SDS-PAGE bands; [b] protein concentration was determined by Bradford assay; [c] protein concentration was determined from the absorbance at 280 nm using the calculated extinction coefficient; [d] values refer to hisPS2 trimer pool that appears as monomer and dimer on 10% SDS-PAGE (Fig. 4a, b); n.d., not determined.

(e)

Step	Volume (ml)	Concentration (mg/ml)	Total Protein (mg)	Purity[a] (%)
Solubilized membrane	100	6.76[b]	676	n.d.
Ni-NTA	25	0.19[c]	4.7	81
First SEC[d]	14	0.13[c]	1.8	95
Second SEC[d]	16	0.10[c]	1.6	96

show different states of the SDS complex of the protein. The appearance of two monomer bands is a typical SDS artifact for membrane proteins when samples are only heated to 46 °C in order to avoid the formation of SDS insoluble aggregates. They are thought to be caused by variations of SDS binding due to the different degrees of denaturation [65]. The appearance of higher molecular weight bands is also regularly observed for membrane proteins under the above-mentioned conditions. For the hisPS2strep construct – which also showed C-terminal completeness on western blots – and the hisPS2 construct, the same behavior on PAGE was observed (Fig. S2).

3.4. Purified hisPS2 is well-folded in FC14 micelles

In order to investigate the secondary structure of purified hisPS2, the protein was subjected to far-UV CD. As shown in Fig. 6a, the CD spectrum at 4 °C displayed one positive peak with a maximum at ~192 nm and two negative peaks with minima at ~209 nm and ~221 nm, which are characteristic for α-helical structures. The spectrum of hisPS2 in the SEC buffer exhibited a similar shape and intensity to the spectrum in the CD buffer above 200 nm. Deconvolution revealed that purified hisPS2 zymogen contained 51.0 ± 1.0% helix and 10.7 ± 0.6% beta-strand, which is in agreement with the secondary structure content predicted by RaptorX (Table 1). The addition of cholesterol does not influence the shape of the CD spectrum or the

Table 1
Secondary structure content of hisPS2.

	4 °C	98 °C	Back to 4 °C	4 °C + CHS	RaptorX
Helix (%)	51.0 ± 1.0	22.0 ± 3.0	28.0 ± 4.6	51.0 ± 2.6	50
Strand (%)	10.7 ± 0.6	29.3 ± 3.5	27.7 ± 4.6	9.7 ± 1.2	8
Turns (%)	13.7 ± 1.5	18.3 ± 6.4	16.3 ± 5.5	14.0 ± 1.0	–
Unordered (%)	25.3 ± n3.2	30.3 ± 3.5	28.0 ± 5.0	26.0 ± 3.5	–
NRMSD ($*E^{-2}$)	1.2 ± 0.3	2.1 ± 0.6	1.3 ± 0.2	1.6 ± 0.2	–

The values represent the mean ± standard deviation from the deconvolution results with reference data sets 4, 7, and SMP 180. NRMSD (normalized root-mean-square deviation) indicates the best fit between the calculated and experimental CD spectra. The secondary structure prediction was performed by RaptorX [89] based on the PS1 structure from cryo-EM (5fn2:B).

secondary structure content (Table 1). After validating the presence of the expected helical content, the tertiary structure was investigated by means of near-UV CD. The near-UV CD spectrum at 4 °C showed two positive defined peaks for phenylalanine centered at 259 nm and 265 nm, respectively. The strong positive peak centered at 292 nm is due to tryptophan absorption. Smaller positive peaks between 270 nm and 282 nm represented the tyrosine absorption (Fig. 7a). The presence of the near-UV CD signal indicated that the secondary structure of purified hisPS2 was folded into a well-defined tertiary structure [66].

Fluorescence emission spectra were recorded to investigate the microenvironment of the aromatic amino acids of hisPS2. As shown in Fig. 5a, the fluorescence spectra with different excitation wavelengths displayed varied intensities with distinctive emission maxima. For excitation wavelengths lower than 285 nm, both tyrosine and tryptophan were excited, while for excitation wavelengths higher than 290 nm, only tryptophan was excited and therefore the intensity was somewhat lower. The fluorescence emission maximum was centered at ~326 nm for excitation wavelengths lower than 285 nm. However, for excitation above 290 nm, the fluorescence emission maximum shifted to ~333 nm (Fig. 5b), which corresponded to tryptophan fluorescence.

3.5. Thermal stability of the secondary and tertiary structure of hisPS2

The thermal stability of the hisPS2 structure was investigated by investigating the structural stability by means of CD-spectroscopy, which is much more sensitive to structural changes than UV/Vis absorption spectroscopy (Fig. 6a, d). Upon heating the secondary and tertiary structure changes can be monitored by CD in the far-UV and the near-UV range, respectively. Unlike the far-UV CD spectrum at 4 °C, the 98 °C spectra displayed a peak minimum at 217 nm, which is characteristic for beta-strand-rich structures (Fig. 6a). The 209:217 nm peak ratio decreased from 1.11 at 4 °C to 0.83 at 98 °C, indicating a loss of helical structure and a gain in beta-strand structure. The 209:217 nm peak ratio from the spectrum after cooling back to 4 °C was 0.90. The presence of an isodichroic point at 200 nm indicated that thermal unfolding is a two-state process. Deconvolution of these spectra showed that the helical content decreased from 51% at 4 °C to 22% at 98 °C, while the beta-strand content increased from 10% to 29% (Table 1). The helical content after cooling back to 4 °C increased only slightly to 28%. Accordingly, a decrease in helical segments or average helix length was accompanied by an increase in strand segments or average strand length (Table 2 in Ref [54]).

The temperature reverse scan revealed that the CD signal at 221 nm did not return to the initial value of the signal at 4 °C when cooling back from 98 °C to 4 °C (Fig. 6b). Fitting the CD signals at 221 nm into a two-state transition revealed T_m values of 53.7, 55.2, and 52.9 °C, respectively, for hisPS2 in CD buffer, SEC buffer, and SEC buffer supplemented with $CaCl_2$. It is interesting to note that although hisPS2 adopted a similar secondary structure in the absence and presence of CHS, FC14-CHS-purified hisPS2 exhibited a T_m value more than 10 °C higher than with FC14 micelle alone (Fig. 6c).

The reliability of the deconvolution depends on the sample concentration. The absorption spectrum (Fig. 6d) before and after thermal unfolding exhibited no significant difference, thus indicating that there was no loss of sample during thermal unfolding due to the precipitation of aggregated protein. Therefore, far-UV CD spectra were deconvoluted reliably to high temperatures. Interestingly, the formation of soluble SDS-resistant oligomers was observed. SDS-PAGE analysis (Fig. 6d, inset) showed that after thermal unfolding, hisPS2 formed SDS-resistant aggregates that did not enter the separation gel. This kind of thermal unfolding-induced aggregation has also been reported for other membrane proteins [67,68].

The tertiary structure stability was investigated by means of near-UV CD spectra. Spectra showed a progressive loss of the CD signal for temperatures from 4 °C to 80 °C (Fig. 7a). The change of the CD signal at 292 nm agreed with a two-state transition model for unfolding with a

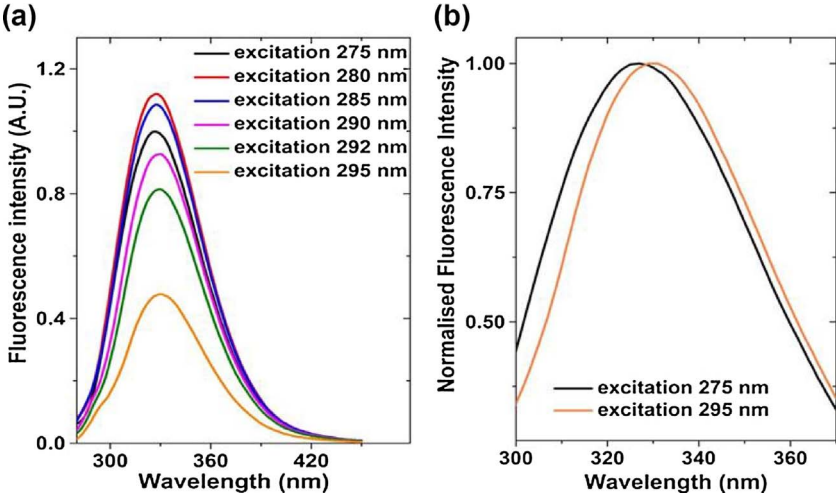

Fig. 5. Intrinsic fluorescence spectra of hisPS2.
(a) HisPS2 fluorescence emission spectra with different excitation wavelengths from 275 nm (both tryptophan and tyrosine are excited) to 295 nm (only tryptophan is excited). (b) Overlay of normalized fluorescence spectra excited at 275 nm and 295 nm to show a ~7 nm shift with emission maximum. This indicates that tyrosine fluorescence is not fully quenched by tryptophan fluorescence, which is in agreement with the expected folding of PSs.

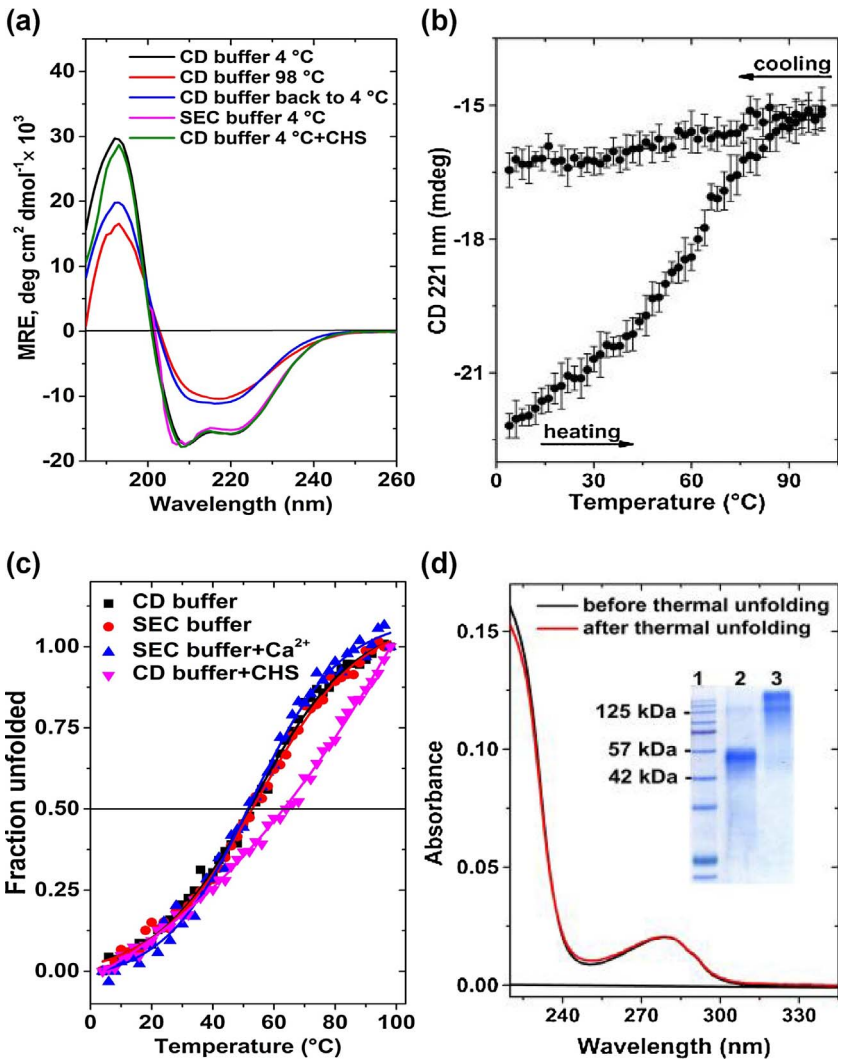

Fig. 6. Thermal stability of the secondary structure of hisPS2.
(a) Overlay of hisPS2 far-UV CD spectra at different temperatures and under different buffer conditions. (b) Thermal unfolding and refolding of hisPS2 in CD buffer monitored by far-UV CD signal at 221 nm as a function of temperature. (c) Thermal unfolding of hisPS2 under different buffer conditions. Solid lines represent the Boltzmann fits. (d) Absorption spectrum before and after thermal unfolding. Inset: 12% SDS-PAGE of the sample before (lane 2) and after thermal unfolding (lane 3); lane 1: prestained protein marker (Jena Bioscience, Jena, Germany).

T_m of 34.2 °C (Fig. 7b). This indicated that the tertiary structure of hisPS2 unfolds earlier than the secondary structure.

3.6. Calcium induces structural change for hisPS2-WT

It was proposed that PSs form passive calcium leakage channels, a function which is independent of γ-secretase activity [28,69,70]. We therefore investigated the effect of calcium on the secondary structure and local differences of hisPS2-WT and hisPS2-D263A/D366A by far-UV CD and intrinsic fluorescence.

As shown in Fig. 8a and b, hisPS2-WT and hisPS2-D263A/D366A exhibited similar far-UV CD spectra. In the presence of calcium, a slight

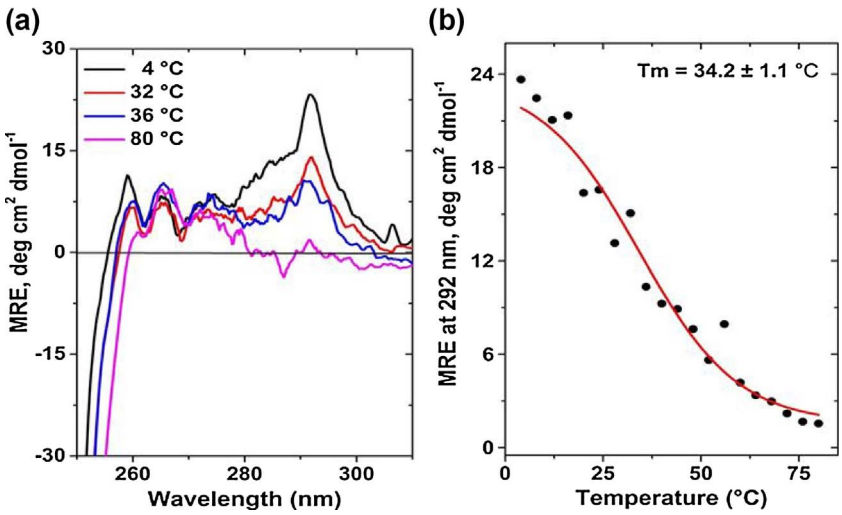

Fig. 7. Thermal stability of the tertiary structure of hisPS2.
(a) Near-UV CD spectra of hisPS2 at 4 °C, 32 °C, 36 °C, and 80 °C. HisPS2 in SEC buffer was unfolded at an increasing temperature. Near-UV CD spectra recorded at different temperatures demonstrated a progressive loss of tertiary structure. (b) Thermal unfolding of hisPS2 tertiary structure monitored by CD signal at 292 nm. Solid line represents the Boltzmann fit.

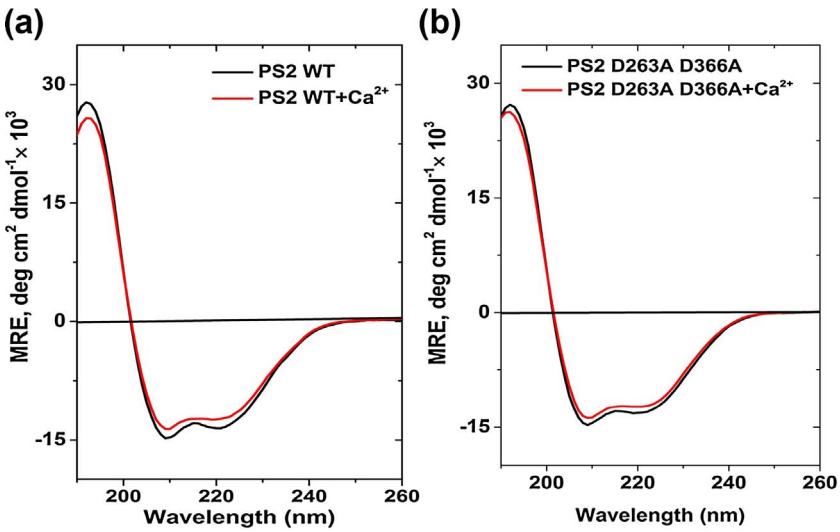

Fig. 8. Effect of calcium ions on the secondary structure and fluorescence of hisPS2.
Purified hisPS2 wild type (PS2 WT) or hisPS2 double mutation (PS2 D263A/D366A) was incubated in the presence or absence of $CaCl_2$ (pro: Ca^{2+} = 1:100 (mol:mol)) at 22 °C for 30 min before being subjected to CD and fluorescence measurements. (a) Far-UV CD spectra of PS2 WT in the presence and absence of Ca^{2+}. (b) Far-UV CD spectra of PS2 D263A/D366A in the presence and absence of Ca^{2+}. (c) Deconvolution of the far-UV CD spectra. (d) Tryptophan fluorescence emission spectrum of PS2WT in the presence and absence of Ca^{2+}. (e) Tryptophan fluorescence emission spectrum of PS2 D263A/D366A in the presence and absence of Ca^{2+}

(c)

Proteins	Helix (%)	Strand (%)	Turns (%)	Unordered (%)	NRMSD (*E^{-2})
PS2 WT	46.7±0.6	12.0±1.0	14.0±1.7	26.3±1.5	1.1±0.2
PS2 WT+Ca^{2+}	43.3±0.6	14.3±0.6	15.0±2.6	26.7±2.1	1.0±0.2
PS2 D263A/D366A	47.3±0.6	11.3±1.2	14.7±1.5	26.3±1.5	1.0±0.3
PS2 D263A/D366A+Ca^{2+}	44.3±0.6	14.3±0.6	14.7±2.5	26.3±1.5	1.1±0.2

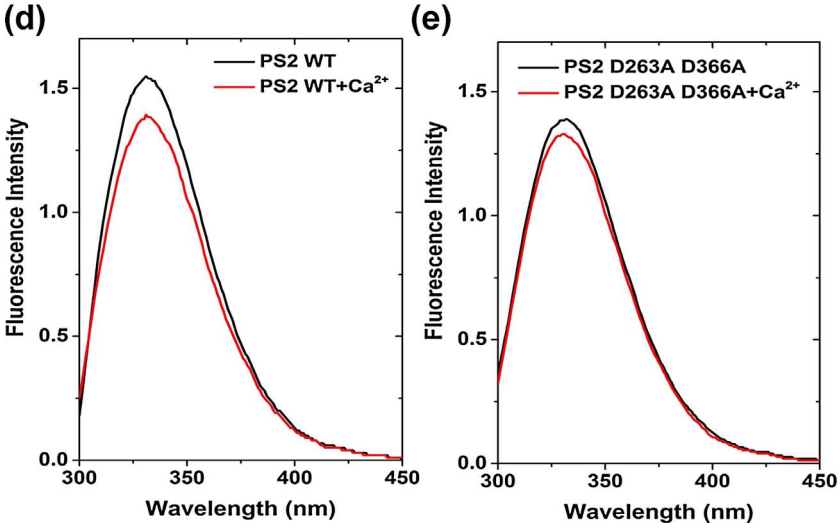

decrease of the "w" shape intensity was detected for both hisPS2-WT and hisPS2-D263A/D366A compared to the corresponding spectra without calcium. Deconvolution (Fig. 8c) revealed that in the presence of calcium, the helical content decreased from 46.7% to 43.3% while the beta-strand content increased from 12.0% to 14.3% for hisPS2-WT. HisPS2-D263A/D366A adopted similar structural changes.

Although hisPS2-D263A/D366A also displayed a secondary structure change in the presence of calcium, the microenvironment of tryptophan residues was evidently different from the wild type. As shown in Fig. 8d and e, hisPS2-D263A/D366A exhibited 10.8% lower fluorescence intensity than hisPS2-WT. In the presence of calcium, the fluorescence was quenched by 11.1% for hisPS2-WT but only 4.2% for hisPS2-D263A/D366A, which demonstrated the different effects of calcium on these proteins.

4. Discussion

Structural investigations of PSs have been mainly focused on cleaved PS1 as the proteolytic subunit of γ-secretase. The investigation of isolated PSs had been limited to the crystal structure of a bacterial homolog and the NMR structure of the PS1 C-terminal fragment due to the low expression level and poor solution behavior of full-length

eukaryotic PSs [48]. The structures of cleaved PS1 were unable to explain the auto-inhibitory and activation mechanism of the PS zymogens, as most of the cytoplasmic loops containing the hydrophobic inhibitory segment and the auto-cleavage sites were not observed [52,71]. Furthermore, it was proposed that the inhibitory loop at the cleavage site plays an important role in the regulation of the suggested calcium leakage channel activity of PSs [72], a function of full-length PSs which is independent of their proteolytic activity [28]. Finally, it was also proposed that the loss of essential functions of PSs alone may be a more potent cause of AD pathogenesis than the accumulation of toxic Aβ peptides [25,26]. Therefore, we aimed to express, purify, and characterize full-length human PS2 zymogen to a sufficient quantity and quality for structural studies.

Upon extensive screening of expression, detergent solubilization, and purification, we overcame the aggregation problem of PS2, and milligram quantities of homogeneous hisPS2 were obtained by a combination of Ni-NTA and SEC. The removal of the periplasmic fraction helped to reduce protein degradation during purification. The ratio of the solubilization buffer to cell pellet amount was found to be crucial for the purity and homogeneity of the purified hisPS2. Less than 5 ml/g cell caused an increase in impurities and poor separation of the two major peaks on SEC. This is likely due to an insufficient number of micelles which caused the co-solubilization of aggregated material. A higher ratio (33 ml/g) only increased the separation slightly, but did not change the ratio of the two peaks significantly (data not shown). These results indicated that hisPS2 existed in FC14 micelles in different oligomerization states. However, it was reported that PS oligomerization is not required for γ-secretase activity [48], although the role of oligomerization for the proposed calcium leakage channel function is unclear. In the absence of other γ-secretase proteins, hisPS2 formed a trimer.

Biophysical characterization revealed that the purified hisPS2 was well-folded. Far-UV CD detected the spectrum for a typical helical protein. Deconvolution indicated that the purified hisPS2 contained the expected amount of the secondary structure (Table 1). Near-UV CD proved that the secondary structure of the purified hisPS2 was folded into a well-defined tertiary structure.

Protein tryptophan fluorescence had emission peaks ranging from 300 nm to 350 nm depending on the polarity of the local environment. The peak maximum at ~333 nm for purified hisPS2 revealed the buried hydrophobic microenvironment of tryptophan side chains [73]. In comparison with PS1, seven of the eight tryptophan residues of PS2 are conserved. They are either located within the transmembrane region (2 in the center, 4 at the ends of TMs) or located within the extra-membrane segment in the big loop between TM6 and TM7 (Fig. S1). The microenvironment of the majority of tryptophan residues were able to explain the observed emission maxima of the tryptophan fluorescence spectra. Protein tyrosine fluorescence is typically undetectable, mainly due to tryptophan residues having much higher absorption coefficients and quantum yields and also due to Förster energy transfer from tyrosine to nearby tryptophan [74]. The distances between tyrosine and nearby tryptophan in the cryo-EM structure of PS1 varied from 5 Å to 23 Å, indicating different energy transfer efficiencies [52]. PS2 contains 22 tyrosine residues, 16 of which are conserved (Fig. S1). For PS2, it is also likely that different energy transfer efficiencies exist between tyrosine and tryptophan. This explains the observation that when exited at 275 nm, hisPS2 exhibited an emission maximum at ~326 nm instead of ~333 nm. The maximum of the fluorescence spectrum shifted to a lower wavelength because the tryptophan fluorescence was overlaid by unquenched tyrosine fluorescence [75]. The intrinsic protein fluorescence spectroscopy thus revealed the expected micro-environment of tryptophan side chains, which is another indicator of proper folding.

It was recently proposed that AD mutations cause AD pathology by impairing the overall protein stability of PS1 [76]. We therefore investigated the thermal stability of the secondary and tertiary structure of hisPS2. The thermal unfolding of hisPS2 in FC14 was an irreversible process, in which part of the helical structure transformed into beta-strand. Cross-beta aggregation prediction by Tango [77]. reveals three regions in PS2 which are aggregation-prone: T142-160Y in TM2, W171-188L in TM3, and F392-409F in TM8 (Fig. S1). Among these three regions, TM2 has the highest aggregation probability, which is in agreement with the observed structural flexibility of PS1 [52,71]. These regions account for 12.2% of the total sequence, which explained the transition from helical to beta-strand structure detected by CD. Such a transition likely causes the formation of the observed heat-stable aggregates by intermolecular beta-strand interaction during thermal unfolding [78]. This is in agreement with the irreversibility of structural transformations of hisPS2 as observed from the temperature reverse scan, the deconvoluted structure composition at different temperatures, and the detection of SDS-resistant aggregates. The presence of 22% helix at 98 °C was probably due to the extreme stability of the detergent-bound helix, which prevented it from unfolding − a phenomenon also observed for other membrane proteins [79,80]. Cholesterol significantly increased the thermal stability of hisPS2, which provides evidence that cholesterol acts as a natural ligand. It was observed that aberrant intracellular cholesterol transport alters PS localization and enhances Aβ production [81,82]. Therefore, cholesterol might regulate Aβ processing by altering the structural stability of PSs. The relatively low T_m value (34.2 °C) of the tertiary structure was in agreement with the reported loose packing of PS1 TMs in the cryo-EM structure [52] and the presence of the interconverting conformations of γ-secretase [83]. Such a T_m value also explained the difficulties (aggregation and impurities) encountered during purification.

For maturation, PSs undergo auto-cleavage within the hydrophobic sequence (E280 to E300 for PS1, E286 to K306 for PS2, Fig. S1) located in the large loop between TM6 and TM7. It was proposed that cleavage removes the inhibitory exon 9 loop which occupies the substrate binding site, thus resulting in an active enzyme [84]. The hydrophobic segment is not only involved in modulating enzyme activation, substrate binding, and processing [84,85], but might also be involved in controlling the potential calcium channel leakage function [72]. Experimental evidence has shown that the PS1-ΔE9 mutant not only exhibited proteolytic activity [86], but also functioned as a calcium leakage channel [28]. The corresponding sequence from the cryo-EM structure of PS1 exhibited a short beta-strand for residues 285–288, while the densities were missing for the rest of the residues [71]. It was proposed that the release of the inhibitory loop (S290 to S319 in PS1) by auto-cleavage after maturation controls both the proteolytic activity and the calcium leakage channel function. The ε-nitrogen of PS1-W294 is in close contact with the nearest δ-oxygen of the catalytic residue PS1-D385 (5 Å) in the immature PSs. This distance increases to > 10 Å in the mature PSs due to the movement of the inhibitory loop out of the proteolytic active site [54]. It is therefore reasonable to assume that after the release of the inhibitory loop, W294 becomes more exposed. However, experimental results showed that the Ca^{2+} channel leakage function of PSs was independent of their proteolytic activity, although residue D385 was indispensable. PS1-D275A abolished proteolytic activity (resulting in uncleaved PSs) but did not influence the Ca^{2+} leakage function while the PS1-D385A mutation lacked both the proteolytic activity and the Ca^{2+} leakage function [69,70,87,88]. In this study, it was observed that hisPS2-WT zymogen underwent conformational changes in the presence of calcium, which suggested that maturation might not be required for the calcium channel function. However, hisPS2-D263A/D366A, which abolishes both the proteolytic activity and the calcium channel function, adopted a different confirmation and exhibited minor structural changes in the presence of calcium. These results are in agreement with the previous experimental observations [28]. W300 in PS2 (Fig. S1), which is located within the inhibiting sequence, might be (partially) responsible for the observed 11% quenching. For hisPS2-D263A/D366A, the quenching decreased to only 4.2%, probably because it adopted a different conformation. Indeed, the quantum yield of hisPS2-D263A/D366A was similar to the

hisPS2-WT in the presence of calcium, thus indicating that W300 might already be more exposed in hisPS2-D263A/D366A than in PS2-WT. The structural changes detected in the presence of calcium for hisPS2-WT probably reflected to some extent the movement of the inhibitory loop, which might open the calcium channel of the PSs. However, knowledge of the actual molecular mechanism of the maturation and calcium channel leakage function of PSs requires the atomic structure of the uncleaved zymogen of PSs.

Conflict of interest

The authors declare that there are no conflicts of interest.

Author contribution

G.Y., K.Y., and J.L. conceived and designed the experiments. J.L. supervised the study. G.Y. performed the experiments. G.Y., K.Y., and J.L. analyzed the data and wrote the manuscript. All authors contributed to the discussion and revision of the manuscript.

Acknowledgements

The study was supported by Forschungszentrum Jülich. Dr. Kun Yu was supported by the China Scholarship Council (CSC). Dr. Jan Kubicek is an employee of Cube Biotech GmbH. We would like to thank Dr. Tino Polen from Forschungszentrum Jülich for helping with the mass spectrometry experiment.

Appendix A. Supplementary data

Supplementary data associated with this article can be found, in the online version, at http://dx.doi.org/10.1016/j.procbio.2017.09.012.

References

[1] W.G. Annaert, L. Levesque, K. Craessaerts, I. Dierinck, G. Snellings, D. Westaway, P.S. George-Hyslop, B. Cordell, P. Fraser, B. De Strooper, Presenilin 1 controls gamma-secretase processing of amyloid precursor protein in pre-golgi compartments of hippocampal neurons, J. Cell Biol. 147 (2) (1999) 277–294.
[2] R. Sannerud, W. Annaert, Trafficking, a key player in regulated intramembrane proteolysis, Semin. Cell Dev. Biol. 20 (2) (2009) 183–190.
[3] S. Prokop, K. Shirotani, D. Edbauer, C. Haass, H. Steiner, Requirement of PEN-2 for stabilization of the presenilin N-/C-terminal fragment heterodimer within the gamma-secretase complex, J. Biol. Chem. 279 (22) (2004) 23255–23261.
[4] B. De Strooper, Aph-1, Pen-2, and Nicastrin with Presenilin generate an active gamma-Secretase complex, Neuron 38 (1) (2003) 9–12.
[5] E.T. Parkin, I. Hussain, E.H. Karran, A.J. Turner, N.M. Hooper, Characterization of detergent-insoluble complexes containing the familial Alzheimer's disease-associated presenilins, J. Neurochem. 72 (4) (1999) 1534–1543.
[6] J.G. Culvenor, G. Evin, M.A. Cooney, H. Wardan, R.A. Sharples, F. Maher, G. Reed, A. Diehlmann, A. Weidemann, K. Beyreuther, C.L. Masters, Presenilin 2 expression in neuronal cells: induction during differentiation of embryonic carcinoma cells, Exp. Cell Res. 255 (2) (2000) 192–206.
[7] M.K. Lee, H.H. Slunt, L.J. Martin, G. Thinakaran, G. Kim, S.E. Gandy, M. Seeger, E. Koo, D.L. Price, S.S. Sisodia, Expression of presenilin 1 and 2 (PS1 and PS2) in human and murine tissues, J. Neurosci. 16 (23) (1996) 7513–7525.
[8] S. Kaja, N. Sumien, V.V. Shah, I. Puthawala, A.N. Maynard, N. Khullar, A.J. Payne, M.J. Forster, P. Koulen, Loss of spatial memory, learning, and motor function during normal aging is accompanied by changes in brain presenilin 1 and 2 expression levels, Mol. Neurobiol. 52 (1) (2015) 545–554.
[9] L. Serneels, J. Van Biervliet, K. Craessaerts, T. Dejaegere, K. Horre, T. Van Houtvin, H. Esselmann, S. Paul, M.K. Schafer, O. Berezovska, B.T. Hyman, B. Sprangers, R. Sciot, L. Moons, M. Jucker, Z. Yang, P.C. May, E. Karran, J. Wiltfang, R. D'Hooge, B. De Strooper, gamma-Secretase heterogeneity in the Aph1 subunit: relevance for Alzheimer's disease, Science 324 (5927) (2009) 639–642.
[10] S.S. Hebert, L. Serneels, T. Dejaegere, K. Horre, M. Dabrowski, V. Baert, W. Annaert, D. Hartmann, B. De Strooper, Coordinated and widespread expression of gamma-secretase in vivo: evidence for size and molecular heterogeneity, Neurobiol. Dis. 17 (2) (2004) 260–272.
[11] M.S. Wolfe, B.A. Yankner, Sorting out presenilins in Alzheimer's disease, Cell 166 (1) (2016) 13–15.
[12] D.R. Dries, G. Yu, Assembly, maturation, and trafficking of the gamma-secretase complex in Alzheimer's disease, Curr. Alzheimer Res. 5 (2) (2008) 132–146.
[13] R. Sannerud, C. Esselens, P. Ejsmont, R. Mattera, L. Rochin, A.K. Tharkeshwar, G. De Baets, V. De Wever, R. Habets, V. Baert, W. Vermeire, C. Michiels, A.J. Groot, R. Wouters, K. Dillen, K. Vints, P. Baatsen, S. Munck, R. Derua, E. Waelkens, G.S. Basi, M. Mercken, M. Vooijs, M. Bollen, J. Schymkowitz, F. Rousseau, J.S. Bonifacino, G. Van Niel, B. De Strooper, W. Annaert, Restricted location of PSEN2/gamma-secretase determines substrate specificity and generates an intracellular abeta pool, Cell 166 (1) (2016) 193–208.
[14] S. Zhang, M. Zhang, F. Cai, W. Song, Biological function of Presenilin and its role in AD pathogenesis, Transl. Neurodegener. 2 (1) (2013) 15.
[15] M. Shih Ie, T.L. Wang, Notch signaling, gamma-secretase inhibitors, and cancer therapy, Cancer Res. 67 (5) (2007) 1879–1882.
[16] T. Iwatsubo, A. Odaka, N. Suzuki, H. Mizusawa, N. Nukina, Y. Ihara, Visualization of A beta 42(43) and A beta 40 in senile plaques with end-specific A beta monoclonals: evidence that an initially deposited species is A beta 42(43), Neuron 13 (1) (1994) 45–53.
[17] J. Hardy, D.J. Selkoe, The amyloid hypothesis of Alzheimer's disease: progress and problems on the road to therapeutics, Science 297 (5580) (2002) 353–356.
[18] D.J. Selkoe, J. Hardy, The amyloid hypothesis of Alzheimer's disease at 25 years, EMBO Mol. Med. 8 (6) (2016) 595–608.
[19] Alzforum, Mutations, http://www.alzforum.org/mutations (Accessed 28.04 2017).
[20] H. Acx, L. Chavez-Gutierrez, L. Serneels, S. Lismont, M. Benurwar, N. Elad, B. De Strooper, Signature amyloid beta profiles are produced by different gamma-secretase complexes, J. Biol. Chem. 289 (7) (2014) 4346–4355.
[21] T. M.T. Borgegård, A. Jureus, J. Malmborg, S. Rosqvist, S. Gruber, A. Almqvist, H. Yan, A. Bogstedt, F. Olsson, J. Dahlström, C. Ray, K. Närhi, D. Malinowsky, E. Hagström, S. Jin, Å. Malm, U. lendahl, J. Lundkvist, In vivo analysis using a presenilin-1-specific inhibitor: presenilin1-containing γ-secretase complexes mediate the majority of CNS Aβ production in the mouse, Alzheimer's Dis. Res. J. 3 (2011) 17.
[22] L. Sun, R. Zhou, G. Yang, Y. Shi, Analysis of 138 pathogenic mutations in presenilin-1 on the in vitro production of Abeta42 and Abeta40 peptides by gamma-secretase, Proc. Natl. Acad. Sci. U. S. A. 114 (4) (2017) E476–E485.
[23] S. Jayadev, J.B. Leverenz, E. Steinbart, J. Stahl, W. Klunk, C.E. Yu, T.D. Bird, Alzheimer's disease phenotypes and genotypes associated with mutations in presenilin 2, Brain 133 (Pt 4) (2010) 1143–1154.
[24] A.J. Larner, Presenilin-1 mutations in Alzheimer's disease: an update on genotype-phenotype relationships, J. Alzheimers Dis. 37 (4) (2013) 653–659.
[25] J. Shen, R.J. Kelleher 3rd, The presenilin hypothesis of Alzheimer's disease: evidence for a loss-of-function pathogenic mechanism, Proc. Natl. Acad. Sci. U. S. A. 104 (2) (2007) 403–409.
[26] D. Xia, H. Watanabe, B. Wu, S.H. Lee, Y. Li, E. Tsvetkov, V.Y. Bolshakov, J. Shen, R.J. Kelleher 3rd, Presenilin-1 knockin mice reveal loss-of-function mechanism for familial Alzheimer's disease, Neuron 15 (5) (2015) 967–981.
[27] F.M. LaFerla, Calcium dyshomeostasis and intracellular signalling in Alzheimer's disease, Nat. Rev. Neurosci. 3 (11) (2002) 862–872.
[28] H. Tu, O. Nelson, A. Bezprozvanny, Z. Wang, S.F. Lee, Y.H. Hao, L. Serneels, B. De Strooper, G. Yu, I. Bezprozvanny, Presenilins form ER Ca2+ leak channels, a function disrupted by familial Alzheimer's disease-linked mutations, Cell 126 (5) (2006) 981–993.
[29] K.H. Cheung, D. Shineman, M. Muller, C. Cardenas, L. Mei, J. Yang, T. Tomita, T. Iwatsubo, V.M. Lee, J.K. Foskett, Mechanism of Ca2+ disruption in Alzheimer's disease by presenilin regulation of InsP3 receptor channel gating, Neuron 58 (6) (2008) 871–883.
[30] D. Shilling, D.O. Mak, D.E. Kang, J.K. Foskett, Lack of evidence for presenilins as endoplasmic reticulum Ca2+ leak channels, J. Biol. Chem. 287 (14) (2012) 10933–10944.
[31] B. Wu, H. Yamaguchi, F.A. Lai, J. Shen, Presenilins regulate calcium homeostasis and presynaptic function via ryanodine receptors in hippocampal neurons, Proc. Natl. Acad. Sci. U. S. A. 110 (37) (2013) 15091–15096.
[32] C. Cai, P. Lin, K.H. Cheung, N. Li, C. Levchook, Z. Pan, C. Ferrante, G.L. Boulianne, J.K. Foskett, D. Danielpour, J. Ma, The presenilin-2 loop peptide perturbs intracellular Ca2+ homeostasis and accelerates apoptosis, J. Biol. Chem. 281 (24) (2006) 16649–16655.
[33] V. Hayrapetyan, V. Rybalchenko, N. Rybalchenko, P. Koulen, The N-terminus of presenilin-2 increases single channel activity of brain ryanodine receptors through direct protein–protein interaction, Cell Calcium 44 (5) (2008) 507–518.
[34] V. Rybalchenko, S.Y. Hwang, N. Rybalchenko, P. Koulen, The cytosolic N-terminus of presenilin-1 potentiates mouse ryanodine receptor single channel activity, Int. J. Biochem. Cell Biol. 40 (1) (2008) 84–97.
[35] K.N. Green, A. Demuro, Y. Akbari, B.D. Hitt, I.F. Smith, I. Parker, F.M. LaFerla, SERCA pump activity is physiologically regulated by presenilin and regulates amyloid beta production, J. Gen. Physiol. 132 (2) (2008) i1.
[36] L. Brunello, E. Zampese, C. Florean, T. Pozzan, P. Pizzo, C. Fasolato, Presenilin-2 dampens intracellular Ca2+ stores by increasing Ca2+ leakage and reducing Ca2+ uptake, J. Cell. Mol. Med. 13 (9B) (2009) 3358–3369.
[37] S.M. Stabler, L.L. Ostrowski, S.M. Janicki, M.J. Monteiro, A myristoylated calcium-binding protein that preferentially interacts with the Alzheimer's disease presenilin 2 protein, J. Cell Biol. 145 (6) (1999) 1277–1292.
[38] K. Shinozaki, K. Maruyama, H. Kume, T. Tomita, T.C. Saido, T. Iwatsubo, K. Obata, The presenilin 2 loop domain interacts with the mu-calpain C-terminal region, Int. J. Mol. Med. 1 (5) (1998) 797–799.
[39] E. Pack-Chung, M.B. Meyers, W.P. Pettingell, R.D. Moir, A.M. Brownawell, I. Cheng, R.E. Tanzi, T.W. Kim, Presenilin 2 interacts with sorcin, a modulator of the ryanodine receptor, J. Biol. Chem. 275 (19) (2000) 14440–14445.
[40] E. Zampese, C. Fasolato, M.J. Kipanyula, M. Bortolozzi, T. Pozzan, P. Pizzo, Presenilin 2 modulates endoplasmic reticulum (ER)-mitochondria interactions and Ca2+ cross-talk, Proc. Natl. Acad. Sci. U. S. A. 108 (7) (2011) 2777–2782.
[41] R. Filadi, E. Greotti, G. Turacchio, A. Luini, T. Pozzan, P. Pizzo, Presenilin 2

modulates endoplasmic reticulum-mitochondria coupling by tuning the antagonistic effect of mitofusin 2, Cell Rep. 15 (10) (2016) 2226–2238.
[42] S.H. Lee, D. Lutz, M. Mossalam, V.Y. Bolshakov, M. Frotscher, J. Shen, Presenilins regulate synaptic plasticity and mitochondrial calcium homeostasis in the hippocampal mossy fiber pathway, Mol. Neurodegener. 12 (1) (2017) 48.
[43] K. Coen, R.S. Flannagan, S. Baron, L.R. Carraro-Lacroix, D. Wang, W. Vermeire, C. Michiels, S. Munck, V. Baert, S. Sugita, F. Wuytack, P.R. Hiesinger, S. Grinstein, W. Annaert, Lysosomal calcium homeostasis defects, not proton pump defects, cause endo-lysosomal dysfunction in PSEN-deficient cells, J. Cell Biol. 198 (1) (2012) 23–35.
[44] K.M. Neely Kayala, G.D. Dickinson, A. Minassian, K.C. Walls, K.N. Green, F.M. Laferla, Presenilin-null cells have altered two-pore calcium channel expression and lysosomal calcium: implications for lysosomal function, Brain Res. 1489 (2012) 8–16.
[45] Z.S. Khachaturian, Hypothesis on the regulation of cytosol calcium concentration and the aging brain, Neurobiol. Aging 8 (4) (1987) 345–346.
[46] I.F. Smith, K.N. Green, F.M. LaFerla, Calcium dysregulation in Alzheimer's disease: recent advances gained from genetically modified animals, Cell Calcium 38 (3–4) (2005) 427–437.
[47] I. Bezprozvanny, M.P. Mattson, Neuronal calcium mishandling and the pathogenesis of Alzheimer's disease, Trends Neurosci. 31 (9) (2008) 454–463.
[48] X. Li, S. Dang, C. Yan, X. Gong, J. Wang, Y. Shi, Structure of a presenilin family intramembrane aspartate protease, Nature 493 (7430) (2013) 56–61.
[49] S. Sobhanifar, B. Schneider, F. Lohr, D. Gottstein, T. Ikeya, K. Mlynarczyk, W. Pulawski, U. Ghoshdastider, M. Kolinski, S. Filipek, P. Guntert, F. Bernhard, V. Dotsch, Structural investigation of the C-terminal catalytic fragment of presenilin 1, Proc. Natl. Acad. Sci. U. S. A. 107 (21) (2010) 9644–9649.
[50] P. Lu, X.C. Bai, D. Ma, T. Xie, C. Yan, L. Sun, G. Yang, Y. Zhao, R. Zhou, S.H. Scheres, Y. Shi, Three-dimensional structure of human gamma-secretase, Nature 512 (7513) (2014) 166–170.
[51] L. Sun, L. Zhao, G. Yang, C. Yan, R. Zhou, X. Zhou, T. Xie, Y. Zhao, S. Wu, X. Li, Y. Shi, Structural basis of human gamma-secretase assembly, Proc. Natl. Acad. Sci. U. S. A. 112 (19) (2015) 6003–6008.
[52] X.C. Bai, C. Yan, G. Yang, P. Lu, D. Ma, L. Sun, R. Zhou, S.H. Scheres, Y. Shi, An atomic structure of human gamma-secretase, Nature 525 (7568) (2015) 212–217.
[53] A. Magnusdottir, I. Johansson, L.G. Dahlgren, P. Nordlund, H. Berglund, Enabling IMAC purification of low abundance recombinant proteins from E. coli lysates, Nat. Methods 6 (7) (2009) 477–478.
[54] G. Yang, K. Yu, K.J., J. Labahn, Data on solubilization, identification and thermal stability of human Presenilin 2, Data in Brief submitted (2017).
[55] M.R. Wilkins, E. Gasteiger, A. Bairoch, J.C. Sanchez, K.L. Williams, R.D. Appel, D.F. Hochstrasser, Protein identification and analysis tools in the ExPASy server, Methods Mol. Biol. 112 (1999) 531–552.
[56] L. Whitmore, B.A. Wallace, Protein secondary structure analyses from circular dichroism spectroscopy: methods and reference databases, Biopolymers 89 (5) (2008) 392–400.
[57] L. Whitmore, B.A. Wallace, DICHROWEB, an online server for protein secondary structure analyses from circular dichroism spectroscopic data, Nucleic Acids Res. 32 (2004) W668–W673 Web Server issue.
[58] S. Wagner, L. Baars, A.J. Ytterberg, A. Klussmeier, C.S. Wagner, O. Nord, P.A. Nygren, K.J. van Wijk, J.W. de Gier, Consequences of membrane protein overexpression in Escherichia coli, Mol. Cell. Proteomics 6 (9) (2007) 1527–1550.
[59] M.M. Klepsch, J.O. Persson, J.W. de Gier, Consequences of the overexpression of a eukaryotic membrane protein, the human KDEL receptor, in Escherichia coli, J. Mol. Biol. 407 (4) (2011) 532–542.
[60] S. Wagner, M.M. Klepsch, S. Schlegel, A. Appel, R. Draheim, M. Tarry, M. Hogbom, K.J. van Wijk, D.J. Slotboom, J.O. Persson, J.W. de Gier, Tuning Escherichia coli for membrane protein overexpression, Proc. Natl. Acad. Sci. U. S. A. 105 (38) (2008) 14371–14376.
[61] E. Siller, D.C. DeZwaan, J.F. Anderson, B.C. Freeman, J.M. Barral, Slowing bacterial translation speed enhances eukaryotic protein folding efficiency, J. Mol. Biol. 396 (5) (2010) 1310–1318.
[62] P.C. Fraering, W. Ye, J.M. Strub, G. Dolios, M.J. LaVoie, B.L. Ostaszewski, A. van Dorsselaer, R. Wang, D.J. Selkoe, M.S. Wolfe, Purification and characterization of the human gamma-secretase complex, Biochemistry 43 (30) (2004) 9774–9789.
[63] C. Gobl, M. Dulle, W. Hohlweg, J. Grossauer, S.F. Falsone, O. Glatter, K. Zangger, Influence of phosphocholine alkyl chain length on peptide-micelle interactions and micellar size and shape, J. Phys. Chem. B 114 (13) (2010) 4717–4724.
[64] A. Rath, F. Cunningham, C.M. Deber, Acrylamide concentration determines the direction and magnitude of helical membrane protein gel shifts, Proc. Natl. Acad. Sci. U. S. A. 110 (39) (2013) 15668–15673.
[65] A. Rath, M. Glibowicka, V.G. Nadeau, G. Chen, C.M. Deber, Detergent binding explains anomalous SDS-PAGE migration of membrane proteins, Proc. Natl. Acad. Sci. U. S. A. 106 (6) (2009) 1760–1765.
[66] S.M. Kelly, N.C. Price, The use of circular dichroism in the investigation of protein structure and function, Curr. Protein Pept. Sci. 1 (4) (2000) 349–384.
[67] M.B. Tol, C. Deluz, G. Hassaine, A. Graff, H. Stahlberg, H. Vogel, Thermal unfolding of a mammalian pentameric ligand-gated ion channel proceeds at consecutive, distinct steps, J. Biol. Chem. 288 (8) (2013) 5756–5769.
[68] K. Yu, G. Yang, J. Labahn, High-efficient production and biophysical characterisation of nicastrin and its interaction with APPC100, Sci. Rep. 7 (2017) 44297.
[69] H. Zhang, S. Sun, A. Herreman, B. De Strooper, I. Bezprozvanny, Role of presenilins in neuronal calcium homeostasis, J. Neurosci. 30 (25) (2010) 8566–8580.
[70] O. Nelson, C. Supnet, A. Tolia, K. Horre, B. De Strooper, I. Bezprozvanny, Mutagenesis mapping of the presenilin 1 calcium leak conductance pore, J. Biol. Chem. 286 (25) (2011) 22339–22347.
[71] X.C. Bai, E. Rajendra, G. Yang, Y. Shi, S.H. Scheres, Sampling the conformational space of the catalytic subunit of human gamma-secretase, Elife 4 (2015).
[72] A.K. Somavarapu, K.P. Kepp, The dynamic mechanism of presenilin-1 function: sensitive gate dynamics and loop unplugging control protein access, Neurobiol. Dis. 89 (2016) 147–156.
[73] Y.K. Reshetnyak, E.A. Burstein, Decomposition of protein tryptophan fluorescence spectra into log-normal components. II. The statistical proof of discreteness of tryptophan classes in proteins, Biophys. J . 81 (3) (2001) 1710–1734.
[74] C. Duy, J. Fitter, How aggregation and conformational scrambling of unfolded states govern fluorescence emission spectra, Biophys. J . 90 (10) (2006) 3704–3711.
[75] H. Edelhoch, R.L. Perlman, M. Wilchek, Tyrosine fluorescence in proteins, Ann. N. Y. Acad. Sci. 158 (1) (1969) 391–409.
[76] A.K. Somavarapu, K.P. Kepp, Loss of stability and hydrophobicity of presenilin 1 mutations causing Alzheimer's disease, J. Neurochem. 137 (1) (2016) 101–111.
[77] R. Linding, J. Schymkowitz, F. Rousseau, F. Diella, L. Serrano, A comparative study of the relationship between protein structure and beta-aggregation in globular and intrinsically disordered proteins, J. Mol. Biol. 342 (1) (2004) 345–353.
[78] A.L. Fink, Protein aggregation: folding aggregates, inclusion bodies and amyloid, Fold. Des. 3 (1) (1998) R9–R23.
[79] K. Charalambous, A.O. O'Reilly, P.A. Bullough, B.A. Wallace, Thermal and chemical unfolding and refolding of a eukaryotic sodium channel, Biochim. Biophys. Acta 1788 (6) (2009) 1279–1286.
[80] J.J. Galka, S.J. Baturin, D.M. Manley, A.J. Kehler, J.D. O'Neil, Stability of the glycerol facilitator in detergent solutions, Biochemistry 47 (11) (2008) 3513–3524.
[81] M. Burns, K. Gaynor, V. Olm, M. Mercken, J. LaFrancois, L. Wang, P.M. Mathews, W. Noble, Y. Matsuoka, K. Duff, Presenilin redistribution associated with aberrant cholesterol transport enhances beta-amyloid production in vivo, J. Neurosci. 23 (13) (2003) 5645–5649.
[82] H. Runz, J. Rietdorf, I. Tomic, M. de Bernard, K. Beyreuther, R. Pepperkok, T. Hartmann, Inhibition of intracellular cholesterol transport alters presenilin localization and amyloid precursor protein processing in neuronal cells, J. Neurosci. 22 (5) (2002) 1679–1689.
[83] N. Elad, B. De Strooper, S. Lismont, W. Hagen, S. Veugelen, M. Arimon, K. Horre, O. Berezovska, C. Sachse, L. Chavez-Gutierrez, The dynamic conformational landscape of gamma-secretase, J. Cell Sci. 128 (3) (2015) 589–598.
[84] K.S. Knappenberger, G. Tian, X. Ye, C. Sobotka-Briner, S.V. Ghanekar, B.D. Greenberg, C.W. Scott, Mechanism of gamma-secretase cleavage activation: is gamma-secretase regulated through autoinhibition involving the presenilin-1 exon 9 loop? Biochemistry 43 (20) (2004) 6208–6218.
[85] K. Ahn, C.C. Shelton, Y. Tian, X. Zhang, M.L. Gilchrist, S.S. Sisodia, Y.M. Li, Activation and intrinsic gamma-secretase activity of presenilin 1, Proc. Natl. Acad. Sci. U. S. A. 107 (50) (2010) 21435–21440.
[86] M.S. Wolfe, W. Xia, B.L. Ostaszewski, T.S. Diehl, W.T. Kimberly, D.J. Selkoe, Two transmembrane aspartates in presenilin-1 required for presenilin endoproteolysis and gamma-secretase activity, Nature 398 (6727) (1999) 513–517.
[87] A. Tolia, L. Chavez-Gutierrez, B. De Strooper, Contribution of presenilin transmembrane domains 6 and 7 to a water-containing cavity in the gamma-secretase complex, J. Biol. Chem. 281 (37) (2006) 27633–27642.
[88] O. Nelson, H. Tu, T. Lei, M. Bentahir, B. de Strooper, I. Bezprozvanny, Familial Alzheimer disease-linked mutations specifically disrupt Ca2+ leak function of presenilin 1, J. Clin. Invest. 117 (5) (2007) 1230–1239.
[89] M. Kallberg, H. Wang, S. Wang, J. Peng, Z. Wang, H. Lu, J. Xu, Template-based protein structure modeling using the RaptorX web server, Nat. Protoc. 7 (8) (2012) 1511–1522.